

論文 / 著書情報
Article / Book Information

Title	Out-of-plane stability assessment of buckling-restrained braces including connections with chevron configuration
Authors	Toru Takeuchi, Ryota Matsui, Saki Mihara
Citation	Earthquake Engineering and Structural Dynamics, Volume 45, 12, pp. 1895-1917
Pub. date	2016, 4
Note	This is the peer reviewed version of the following article: Earthquake Engineering and Structural Dynamics, Volume 45, 12, pp. 1895-1917, which has been published in final form at http://dx.doi.org/10.1002/eqe.2724 . This article may be used for non-commercial purposes in accordance with Wiley Terms and Conditions for Self-Archiving.

Out-of-Plane Stability Assessment of Buckling-Restrained Braces including Connections with Chevron Configuration

Toru Takeuchi ^{1*}, Ryota Matsui¹, Saki Mihara²

¹*Department of Architecture and Building Engineering, Tokyo Institute of Technology, Tokyo, Japan*

²*Former graduate student, Tokyo Institute of Technology, Tokyo, Japan*

SUMMARY

One of the key limit states of Buckling-restrained braces (BRBs) is global flexural buckling including the effects of the connections. The authors have previously proposed a unified explicit equation set for controlling the out-of-plane stability of BRBs based on bending-moment transfer capacity at the restrainer ends. The proposed equation set is capable of estimating BRB stability for various connection stiffness, including initial out-of-plane drift effects. However, it is only valid for symmetrical end conditions, limiting application to the single diagonal configuration. In the chevron configuration, the out-of-plane stiffness in the two ends differs because of the rotation of the attached beam. In this study, the equation set is extended to BRBs with asymmetric end conditions, such as the chevron configuration. Cyclic loading tests of the chevron configuration with initial out-of-plane drifts are conducted, and the results compared with the proposed equation set, which is formulated as a function of the normalized stiffness of the attached beam.

KEY WORDS: Buckling-restrained brace, Connections, Chevron configuration, Cyclic loading test, Moment transfer capacity, Mechanical stability

1. INTRODUCTION

One key factor that influences the seismic performance of buckling-restrained braces is the global flexural buckling. In the past 25 years, numerous researchers have conducted experiments and numerical analysis on BRBs to establish a method of avoiding global flexural buckling and ensuring stable hysteresis. However, the critical aspect of BRB performance requires inclusion of the connection effect in the assessment of the buckling failure mode. Takeuchi et al. [1] summarized the most recent literature related to connection failure, which includes research highlights [2–14] and the steel structure seismic provisions [15–16]. Additionally, Lin et al. [17] investigated the connection stress distribution by means of experimental testing and FEM analysis, proposing several design recommendations. Zhao et al. [18] proposed a practical design method to ensure the global stability of the BRBs based on a moment amplification factor, in order to simplify the effect of connections. Bruneau et al. [19] suggested evaluation of BRB connection buckling strength by Euler buckling, taking the equivalent length as twice the connection length. This is based on the assumption that the ends are rotationally rigid, idealizing the connection as a cantilever. However, this assumption is optimistic in actual conditions, as the effect of end rotations is not negligible, especially in chevron configurations.

The previous studies have treated the restrainer-ends as pin connections, and the gusset plates ends as rotationally fixed. However, the bending-moment transfer capacity at the restrainer ends and gusset plate rotational stiffness significantly affects the global stability of BRBs. Additionally, these past studies have generally not considered the effects of story drift in

the out-of-plane direction. Although Palmer et al. [20] carried out bi-directional tests on pin-ended BRBs, effects on bolted BRBs were not clarified. These shortcomings were addressed by the author's previously proposed method [1], namely a more rigorous treatment of boundary conditions including bending moment transfer-capacity at the restrainer ends and initial imperfections due to bi-directional effects. The authors discussed the stability requirements for BRBs in a one-way configuration, including the aforementioned conditions, and proposed a simple set of equations. As part of that study, the authors performed cyclic axial loading tests on BRBs with an initial out-of-plane drift and verified the accuracy of the proposed equation set. However, the proposed equations are derived under the condition that the same connections exist at both ends, a condition which is applicable only for certain one-way configurations (Figure 1(a)). In the present study, the equation set is extended to BRBs in a chevron configuration (Figure 1(b)) with asymmetrical end conditions, and a general stability evaluation method for BRBs is proposed. A series of cyclic loading tests on BRBs in a chevron configuration (Figure 1(c)) is conducted, and the results are compared with those obtained using the proposed extended equations.

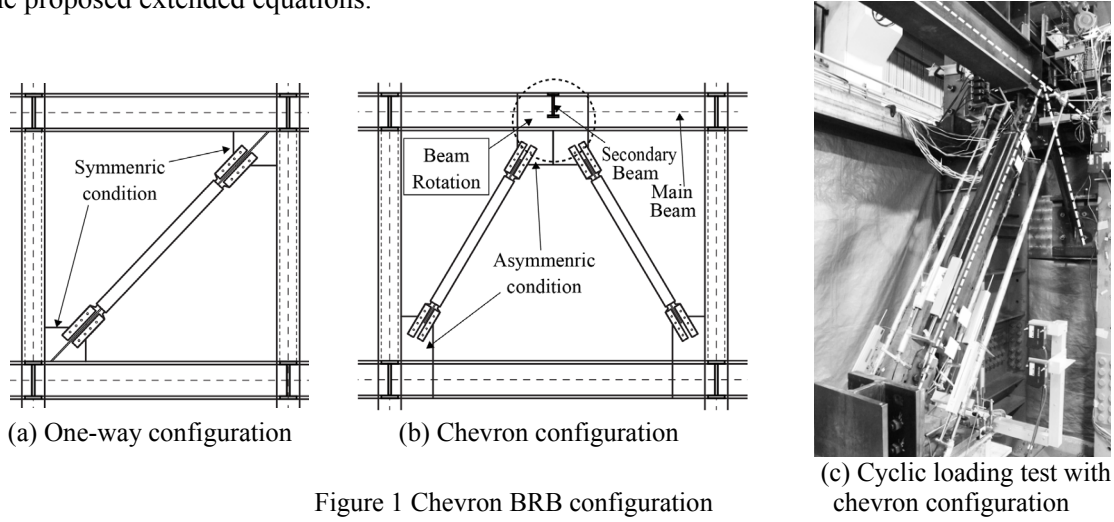


Figure 1 Chevron BRB configuration

2 STABILITY LIMITS UNDER ASYMMETRICAL CONDITIONS

The authors have proposed the following equations to evaluate the stability limit of BRBs, including the connection effect. The stability limit axial force, N_{lim1} , is expressed as follows [1], which needs to be larger than the maximum yield axial force of the core member, N_{cu} .

$$N_{lim1} = \frac{(M_p^r - M_0^r)/a_r + N_{cr}^r}{(M_p^r - M_0^r)/(a_r N_{cr}^B) + 1} > N_{cu} \quad (1)$$

Here, M_p^r denotes the moment transfer capacity at the restrainer end and M_0^r denotes the initial bending moment at the restrainer ends produced by out-of-plane drift (Appendix A). a_r denotes the initial imperfection at the restrainer ends, which can be estimated as $a_r = a_t + e + s_r + (2s_r/L_{in})\xi L_0$, and is shown in Fig. 2 in the Notations. N_{cr}^B denotes the global elastic buckling strength of a BRB, including the effects of the bending stiffness of the connection zone and the rotational stiffness of gusset plates (Appendix B). The difference of $(M_p^r - M_0^r)$ is assumed as zero for negative values. N_{cr}^r is the buckling strength of connections, where the bending-moment transfer capacity at the restrainer ends is not considered. In the elastic range with fixed end rotations, this value is estimated as $N_{cr}^r = \pi^2 \gamma_j EI_B / (2\xi L_0)^2$. In the elasto-plastic range with end rotational springs, N_{cr}^r can be evaluated by substituting the equivalent slenderness ratio, given in Equation (2), into the

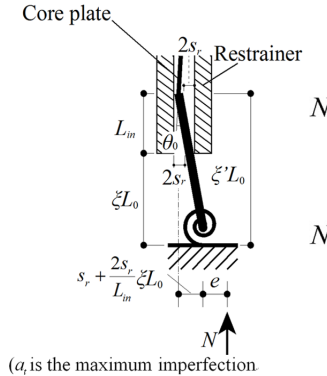


Figure 2 Initial imperfection
(a_r is the maximum imperfection along the restrainer)

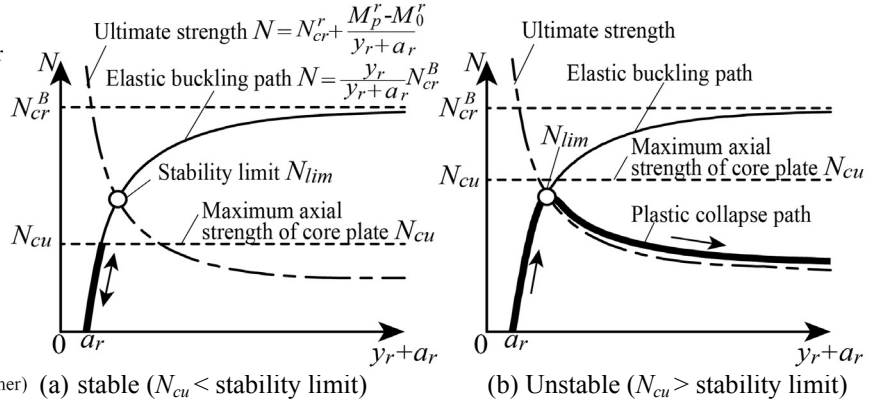


Figure 3 Stability concepts and limits

various elasto-plastic design column curves.

$$\lambda_r = \frac{2\xi L_0}{i_c} \cdot \sqrt{\frac{\xi K_{Rg} + 24/\pi^2}{(1-2\xi)\xi K_{Rg}}} \quad (2)$$

Here, ξL_0 is the connection length, i_c is the radius of gyration in the connection zone, ξK_{Rg} is the normalized rotational stiffness at the outer ends of the connections given by $\xi K_{Rg} = (K_{Rg} \xi L_0) / (\gamma_J EI_B)$, and K_{Rg} is the rotational stiffness of the gusset plate. When the moment transfer capacity $M_p^r = 0$ and ξK_{Rg} is infinity, Equations (1) and (2) give the same criteria as Bruneau et al. [19]. However, as reported in Ida et al. [21], ξK_{Rg} is distributed between 0.2 and 1.0 in actual connections, and the effective buckling length becomes larger than twice the connection length.

Similar to Equation (1), under the assumption that plastic hinges are created at the gusset plates, the expected limit axial force, N_{lim2} , is proposed as follows [1]:

$$N_{lim2} = \frac{\left[\{(1-2\xi)M_p^g - M_0^r\} + (M_p^r - M_0^r) \right] / a_r}{\left[\{(1-2\xi)M_p^g - M_0^r\} + (M_p^r - M_0^r) \right] / (a_r N_{cr}^B) + 1} > N_{cu}, \quad (3)$$

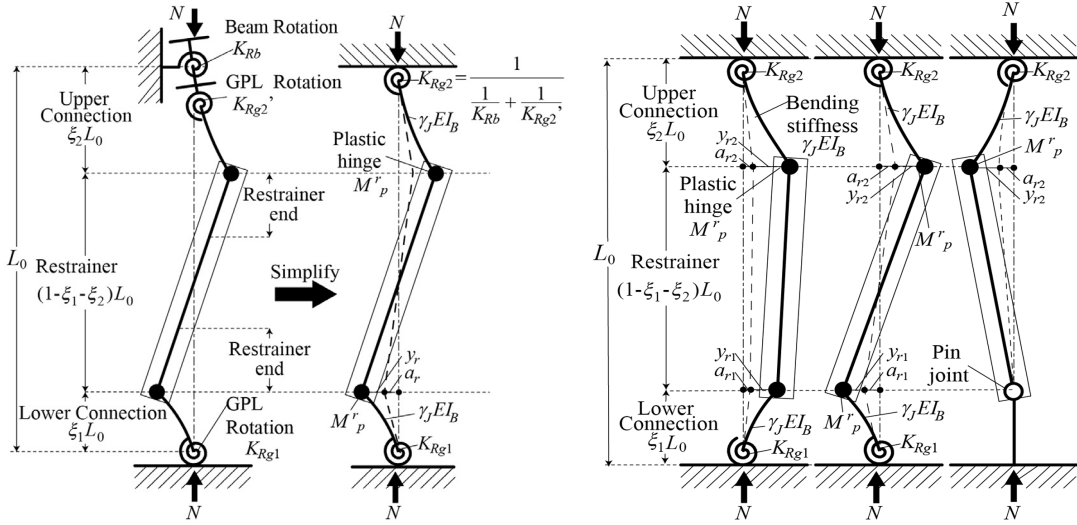
where M_p^g is the plastic bending strength of the gusset plate including the axial force effect. $[(1-2\xi)M_p^g - M_0^r]$ or $[M_p^r - M_0^r]$ should be taken as zero if the difference is negative.

The smaller of the two limit forces obtained from Equations (1) and (3) becomes the stability limit axial force, N_{lim} , and the BRB is considered to be stable where N_{lim} is larger than the maximum yielding force of the core, N_{cu} . These equations have been derived from the intersection of the elastic buckling path and ultimate strength curve as shown in Figure 3. The elastic buckling path can be defined as follows:

$$N = \frac{y_r}{y_r + a_r} N_{cr}^B, \quad (4)$$

where y_r denotes out-of-plane deformation at restrainer ends, and N_{cr}^B denotes the global elastic BRB buckling strength, including the effects of the connection zone's bending stiffness and the gusset plates' rotational stiffness. This can be evaluated by the method in Appendix B.

The above equations are applicable under the condition that the connection length ratio, ξ , and the normalized rotational stiffness, ξK_{Rg} , are the same at both ends. However, this condition is not satisfied in the chevron configuration because the upper beam cannot be assumed as rigid



(a) GPL springs with beam spring (b) equivalent spring at the beam center
Figure 4 Collapse model for chevron configuration

(a) symmetric, (b) asymmetric, (c) one-sided rotational springs
Figure 5 Collapse mechanism modes with rotational springs

(Figure 4 (a)). In this configuration, the equivalent connection length ratio becomes larger and the rotational stiffness becomes smaller, due to the rotation of the connected beam. The length of the upper connection, $\xi_2 L_0$, is measured from the cross-sectional center of the beam, while the rotational stiffness is expressed by the following Equation (5), and shown in Figure 4 (b).

$$K_{Rg2} = \frac{1}{(1/K_{Rb}) + (1/K'_{Rg2})} \quad (5)$$

$$\xi K_{Rg1} = \frac{K_{Rg1} \xi_1 L_0}{\gamma_J EI_B}, \quad \xi K_{Rg2} = \frac{K_{Rg2} \xi_2 L_0}{\gamma_J EI_B} \quad (6)$$

Here, K_{Rb} is the rotational stiffness of the beam about the brace major axis with the brace bending in the out-of-plane direction, and K'_{Rg2} is the rotational stiffness of the upper gusset plate. When the rotational stiffness of the lower gusset plate at the column–beam joint is defined as K_{Rg1} , the normalized rotational stiffness at both ends can be defined as Equation (6).

The ultimate strength, which is based on the asymmetrical conditions shown in Figure 5, is calculated based on an approach similar to that of the previous study [1]. First, in the symmetric collapse mode in Figure 5(a), the gusset plates are assumed to be rigid ($K_{Rg1}, K_{Rg2} \rightarrow \infty$), and out-of-plane deformation of the connection zones is idealized as a sinusoidal shape, as shown in the Figure and given in Equations (7) and (8):

$$y_1 = a_{r1} \frac{x}{\xi_1 L_0} + y_{r1} \left\{ 1 - \cos \left(\frac{\pi}{2} \frac{x}{\xi_1 L_0} \right) \right\} \quad (7)$$

$$y_2 = a_{r2} \frac{x}{\xi_2 L_0} + y_{r2} \left\{ 1 - \cos \left(\frac{\pi}{2} \frac{x}{\xi_2 L_0} \right) \right\} \quad (8)$$

where y_{r1} and y_{r2} denote the out-of-plane deformation at the lower and upper restrainer ends, respectively. Similarly, a_{r1} and a_{r2} denote the imperfections at the lower and upper restrainer ends. The flexural strain energy stored in each connection zone is then given as follows:

$$U_{\varepsilon 1} = \frac{\gamma_J EI_B}{2} \int_0^{\xi_1 L_0} \left(\frac{d^2}{dx^2} \left(y_{r1} - \frac{a_{r1}}{\xi_1 L_0} \right) \right)^2 dx = \frac{\pi^4 \gamma_J EI_B y_{r1}^2}{64 (\xi_1 L_0)^3} \quad (9)$$

$$U_{\varepsilon 2} = \frac{\gamma_J EI_B}{2} \int_0^{\xi_2 L_0} \left(\frac{d^2}{dx^2} \left(y_{r2} - \frac{a_{r2}}{\xi_2 L_0} \right) \right)^2 dx = \frac{\pi^4 \gamma_J EI_B y_{r2}^2}{64 (\xi_2 L_0)^3} \quad (10)$$

Including the reduction due to the rotational springs at each gusset plate, the total flexural strain energy from the connection zones can be assumed as follows:

$$U_\varepsilon = U_{\varepsilon 1} + U_{\varepsilon 2} = \frac{\gamma_J EI_B \pi^4}{64 L_0^3} \left\{ \frac{y_{r1}^2}{\xi_1^3} \left(\frac{\xi \mathcal{K}_{Rg1}}{\xi \mathcal{K}_{Rg1} + 3} \right)^2 + \frac{y_{r2}^2}{\xi_2^3} \left(\frac{\xi \mathcal{K}_{Rg2}}{\xi \mathcal{K}_{Rg2} + 3} \right)^2 \right\} \quad (11)$$

Note that in Equation (11), the bending deformations of the connection zone becomes equal to rotational deformation of the end spring when $\xi \mathcal{K}_{Rg} = 3$ [1]. The rotation angle of the lower and upper plastic hinges at the restrainer ends is expressed as follows:

$$\Delta\theta_{r1} = \frac{\pi y_{r1}}{2 \xi_1 L_0} \frac{\xi \mathcal{K}_{Rg1}}{\xi \mathcal{K}_{Rg1} + 3} + \frac{y_{r1}}{\xi_1 L_0} \frac{3}{\xi \mathcal{K}_{Rg1} + 3} = \frac{y_{r1} (\pi \xi \mathcal{K}_{Rg1} + 6)}{2 \xi_1 L_0 (\xi \mathcal{K}_{Rg1} + 3)} \quad (12)$$

$$\Delta\theta_{r2} = \frac{y_{r2} (\pi \xi \mathcal{K}_{Rg2} + 6)}{2 \xi_2 L_0 (\xi \mathcal{K}_{Rg2} + 3)} \quad (13)$$

Then, the plastic strain energy stored in the plastic hinges is calculated as follows:

$$U_p = M_p^r \Delta\theta_{r1} + M_p^r \Delta\theta_{r2} = \frac{M_p^r}{2 L_0} \left\{ \frac{y_{r1} (\pi \xi \mathcal{K}_{Rg1} + 6)}{\xi_1 (\xi \mathcal{K}_{Rg1} + 3)} + \frac{y_{r2} (\pi \xi \mathcal{K}_{Rg2} + 6)}{\xi_2 (\xi \mathcal{K}_{Rg2} + 3)} \right\} \quad (14)$$

The lower gusset plate spring rotation, $\Delta\theta_{s1}$, the upper gusset plate spring rotation, $\Delta\theta_{s2}$, and their strain energy, U_s , can be expressed as follows:

$$\Delta\theta_{s1} = \frac{y_{r1}}{\xi_1 L_0} \frac{3}{\xi \mathcal{K}_{Rg1} + 3}, \quad \Delta\theta_{s2} = \frac{y_{r2}}{\xi_2 L_0} \frac{3}{\xi \mathcal{K}_{Rg2} + 3} \quad (15)$$

$$U_s = \frac{1}{2} K_{Rg1} \Delta\theta_{s1}^2 + \frac{1}{2} K_{Rg2} \Delta\theta_{s2}^2 = \frac{\gamma_J EI_B}{2} \left[\frac{\xi \mathcal{K}_{Rg1}}{\xi_1 L_0} \left(\frac{y_{r1}}{\xi_1 L_0} \frac{3}{\xi \mathcal{K}_{Rg1} + 3} \right)^2 + \frac{\xi \mathcal{K}_{Rg2}}{\xi_2 L_0} \left(\frac{y_{r2}}{\xi_2 L_0} \frac{3}{\xi \mathcal{K}_{Rg2} + 3} \right)^2 \right] \quad (16)$$

The axial deformation, Δu_g , is then calculated from Equation (17) using the approximation $\pi^2/8 \approx 1$.

$$\Delta u_g \approx \frac{1}{2 \xi_1 L_0} (y_{r1}^2 + 2 a_{r1} y_{r1}) \left(\frac{3}{\xi \mathcal{K}_{Rg1} + 3} + \frac{\pi^2}{8} \frac{\xi \mathcal{K}_{Rg1}}{\xi \mathcal{K}_{Rg1} + 3} \right) + \frac{1}{2 \xi_2 L_0} (y_{r2}^2 + 2 a_{r2} y_{r2}) \left(\frac{3}{\xi \mathcal{K}_{Rg2} + 3} + \frac{\pi^2}{8} \frac{\xi \mathcal{K}_{Rg2}}{\xi \mathcal{K}_{Rg2} + 3} \right) \quad (17)$$

Assuming $a_{r2} = a_r$, $a_{r1} = r_a a_r$, $y_{r2} = y_r$, and $y_{r1} = r_a y_r$, the external work T is estimated from Equation (18).

$$T \approx \frac{y_r^2 + 2 a_r y_r}{2 L_0} \times \left(\frac{r_a^2}{\xi_1} \left(\frac{\pi^2}{8} \frac{\xi \mathcal{K}_{Rg1}}{\xi \mathcal{K}_{Rg1} + 3} + \frac{3}{\xi \mathcal{K}_{Rg1} + 3} \right) + \frac{1}{\xi_2} \left(\frac{\pi^2}{8} \frac{\xi \mathcal{K}_{Rg2}}{\xi \mathcal{K}_{Rg2} + 3} + \frac{3}{\xi \mathcal{K}_{Rg2} + 3} \right) \right) \cdot N \quad (18)$$

With the balance of energy differential $\partial(U_\varepsilon + U_s + U_p - T) / \partial y_r = 0$,

$$\begin{aligned} & \frac{\partial(U_\varepsilon + U_p + U_s - T)}{\partial y_r} \\ &= \frac{\gamma_J EI_B \pi^4}{32 L_0^3} \left\{ \frac{r_a^2}{\xi_1^3} \left(\frac{\xi \mathcal{K}_{Rg1}}{\xi \mathcal{K}_{Rg1} + 3} \right)^2 + \frac{1}{\xi_2^3} \left(\frac{\xi \mathcal{K}_{Rg2}}{\xi \mathcal{K}_{Rg2} + 3} \right)^2 \right\} + \frac{M_p^r}{2 L_0} \left\{ \frac{r_a (6 + \pi \xi \mathcal{K}_{Rg1})}{\xi_1 (\xi \mathcal{K}_{Rg1} + 3)} + \frac{(6 + \pi \xi \mathcal{K}_{Rg2})}{\xi_2 (\xi \mathcal{K}_{Rg2} + 3)} \right\} \\ &+ \frac{9 \gamma_J EI_B y_r}{L_0^3} \left\{ \frac{r_a^2 \xi \mathcal{K}_{Rg1}}{\xi_1^3 (\xi \mathcal{K}_{Rg1} + 3)^2} + \frac{\xi \mathcal{K}_{Rg2}}{\xi_2^3 (\xi \mathcal{K}_{Rg2} + 3)^2} \right\} - \frac{y_r + a_r}{L_0} \left(\frac{r_a^2}{\xi_1} \left(\frac{\xi \mathcal{K}_{Rg1} \pi^2 / 8 + 3}{\xi \mathcal{K}_{Rg1} + 3} \right) + \frac{1}{\xi_2} \left(\frac{\xi \mathcal{K}_{Rg2} \pi^2 / 8 + 3}{\xi \mathcal{K}_{Rg2} + 3} \right) \right) \cdot N \\ &= 0 \end{aligned} \quad (19)$$

From Equation (19), we obtain the formula of N as a function of M_p^r , $\xi\kappa_{Rg1}$, $\xi\kappa_{Rg2}$, ξ_1 , and ξ_2 . By reducing the moment transfer-capacity, M_p^r , by the out-of-plane drift induced moment, M_0^r , as same in the previous study [1], the ultimate strength of the BRBs can be expressed as follows:

$$N = N_{cr}^r + \beta \frac{M_p^r - M_0^r}{y_r + a_r}, \quad \beta = \frac{4}{\pi} \cdot \frac{\frac{r_a}{\xi_1} \frac{\xi\kappa_{Rg1} + 6/\pi}{\xi\kappa_{Rg1} + 3} + \frac{1}{\xi_2} \frac{\xi\kappa_{Rg2} + 6/\pi}{\xi\kappa_{Rg2} + 3}}{\frac{r_a^2}{\xi_1} \frac{\xi\kappa_{Rg1} + 24/\pi^2}{\xi\kappa_{Rg1} + 3} + \frac{1}{\xi_2} \frac{\xi\kappa_{Rg2} + 24/\pi^2}{\xi\kappa_{Rg2} + 3}} \approx 1 \quad (20)$$

$$N_{cr}^r = \frac{\pi^2 \gamma_J EI_B}{(2L_0)^2} \frac{\frac{r_a^2}{\xi_1} \frac{\xi\kappa_{Rg1}}{\xi\kappa_{Rg1} + 3} + \frac{\xi\kappa_{Rg2}}{\xi_2^3 (\xi\kappa_{Rg2} + 3)}}{\frac{r_a^2}{\xi_1} \frac{\xi\kappa_{Rg1} + 24/\pi^2}{\xi\kappa_{Rg1} + 3} + \frac{1}{\xi_2} \frac{\xi\kappa_{Rg2} + 24/\pi^2}{\xi\kappa_{Rg2} + 3}} \quad (21)$$

By a similar process, in the asymmetrical collapse mode in Figure 5(b), Equation (21) becomes

$$N_{cr}^r = \frac{\pi^2 \gamma_J EI_B}{(2L_0)^2} \frac{C_2}{C_1}, \quad C_2 = \frac{r_a^2}{\xi_1^3 (\xi\kappa_{Rg1} + 3)} + \frac{\xi\kappa_{Rg2}}{\xi_2^3 (\xi\kappa_{Rg2} + 3)},$$

$$C_1 = \frac{(\xi\kappa_{Rg1} + 24/\pi^2)(r_a^2 + r_a \xi_1 - r_a^2 \xi_2)}{\xi_1 (1 - \xi_1 - \xi_2)(\xi\kappa_{Rg1} + 3)} + \frac{(\xi\kappa_{Rg2} + 24/\pi^2)(1 + r_a \xi_2 - \xi_1)}{\xi_2 (1 - \xi_1 - \xi_2)(\xi\kappa_{Rg2} + 3)} \quad (22)$$

For the one-sided collapse mode shown in Figure 5(c), Equation (21) becomes

$$N_{cr}^r = \frac{\pi^2 (1 - \xi_1 - \xi_2) \gamma_J EI_B}{(2\xi_2 L_0)^2} \frac{\xi\kappa_{Rg2}}{(1 - \xi_1)(\xi\kappa_{Rg2} + 24/\pi^2)} \quad (23)$$

Comparing Equations (21), (22), and (23), the minimum N_{cr}^r is determined by the asymmetrical or one-sided mode. As a result, the stability limit—determined by the cross point of Equation (4) and Equation (20)—can be expressed as Equation (1).

$$N_{lim1} = \frac{(M_p^r - M_0^r)/a_r + N_{cr}^r}{(M_p^r - M_0^r)/(a_r N_{cr}^B) + 1} > N_{cu} \quad (1)$$

N_{cr}^r can be obtained using the equivalent slenderness ratio, given as follows:

$$\lambda_r = \frac{2L_0}{i_c} \cdot \sqrt{\frac{C_1}{C_2}} \quad (\text{Asymmetrical mode}) \quad (24)$$

$$\lambda_r = \frac{2\xi_2 L_0}{i_c} \sqrt{\frac{(1 - \xi_1)(\xi\kappa_{Rg2} + 24/\pi^2)}{(1 - \xi_1 - \xi_2)\xi\kappa_{Rg2}}} \quad (\text{One-sided mode}) \quad (25)$$

C_1 and C_2 in Equation (24) are defined in Equation (22).

Furthermore, the stability limit with plastic hinges at the gusset plates, N_{lim2} , can be expressed as follows:

$$N_{lim2} = \frac{(M_p^r - M_0^r + C_3)/a_r}{(M_p^r - M_0^r + C_3)/(a_r N_{cr}^B) + 1}, \quad C_3 = \left(\frac{M_p^{g1} - M_0^r}{\xi_1} + \frac{M_p^{g2} - M_0^r}{\xi_2} \right) \frac{1}{1/\xi_1 + 1/\xi_2 + 4/(1 - \xi_1 - \xi_2)}$$

(Asymmetrical mode) (26)

$$N_{lim2} = \frac{\left[(1 - \xi_1 - \xi_2)(M_p^{g2} - M_0^r)/(1 - \xi_1) + M_p^r - M_0^r \right]/a_r}{\left[(1 - \xi_1 - \xi_2)(M_p^{g2} - M_0^r)/(1 - \xi_1) + M_p^r - M_0^r \right]/(a_r N_{cr}^B) + 1} \quad (\text{One-sided mode}) \quad (27)$$

It can easily be confirmed that Equations (24) and (26) become Equations (2) and (3), respectively, when $\xi_1 = \xi_2$, $\xi K_{Rg1} = \xi K_{Rg2}$ and $r_a = 1$.

3 CYCLIC BRB LOADING TESTS WITH CHEVRON CONFIGURATION

To validate the proposed stability equations, cyclic loading tests were performed on BRBs in a chevron configuration, including initial out-of-plane drifts. The test program simulated the worst-case scenario, in which the maximum in-plane story drift occurs at the same time as the 1% out-of-plane story drift. The test configuration with the specimen is shown in Figures 6–9, and the test matrix is summarized in Table 1. The core plate material was JIS-SN400B (average yield

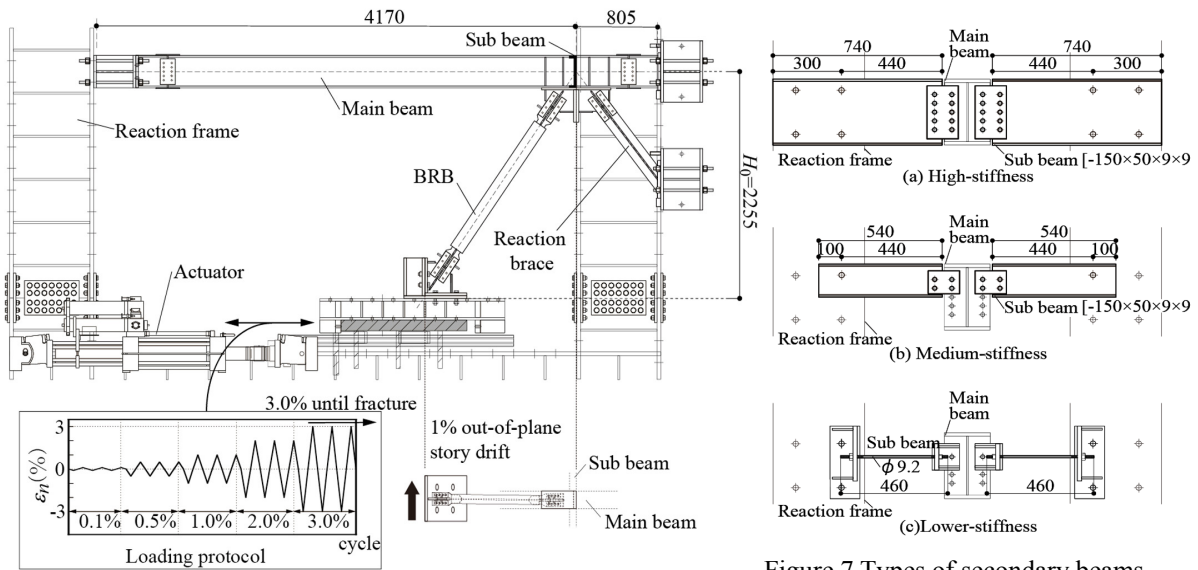


Figure 6 Test setup and loading protocol

Figure 7 Types of secondary beams

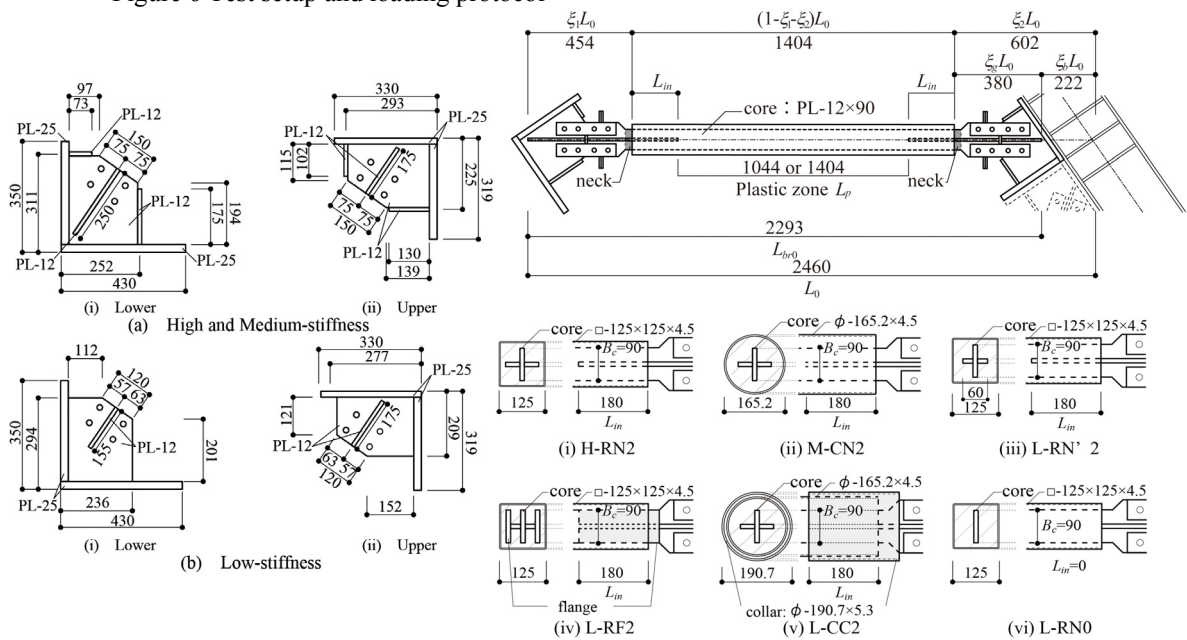


Figure 8 Types of gusset plates (mm)

Figure 9 BRB specimens with various restrainer ends (mm)

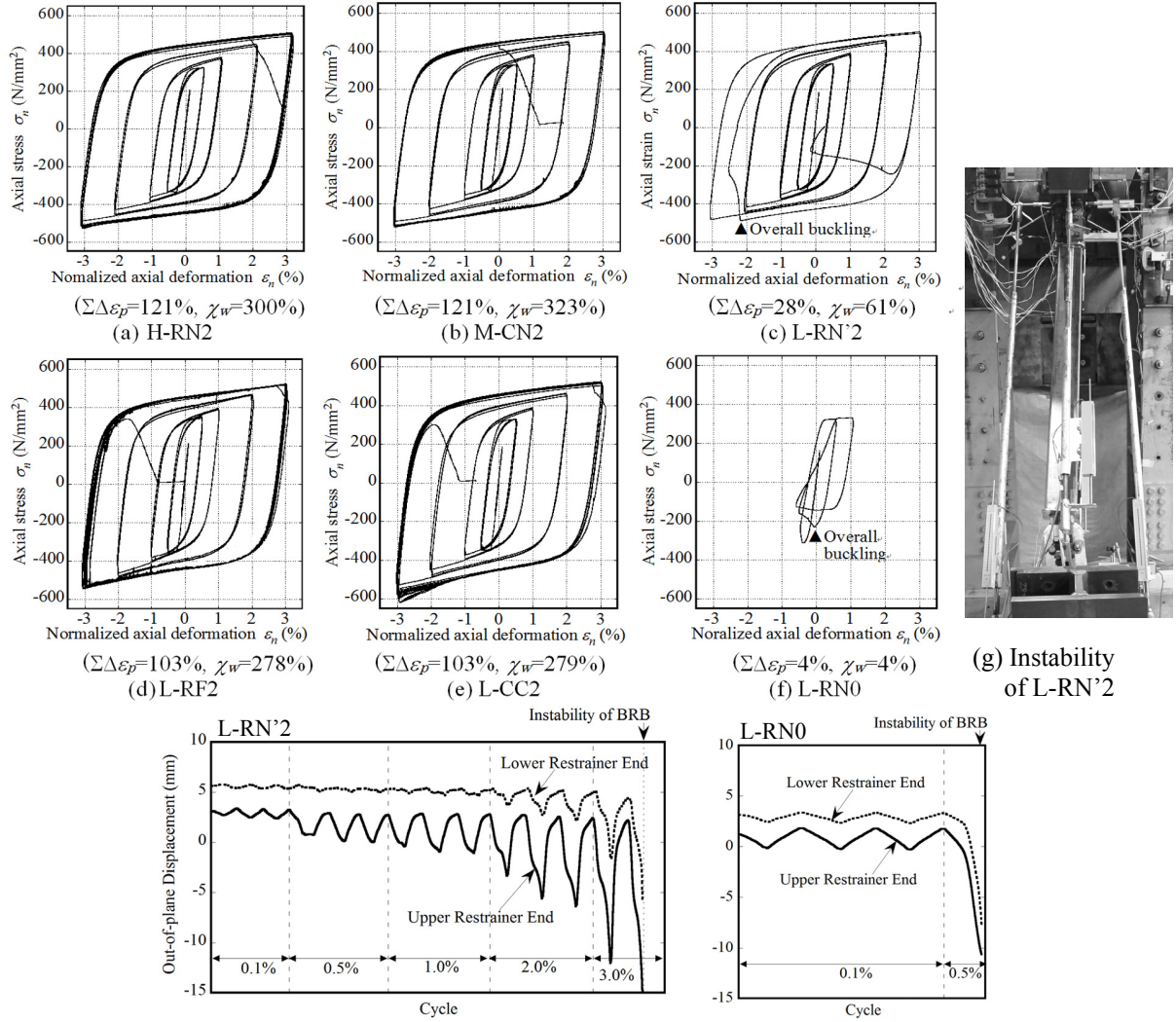
Table 1. Test matrix

Specimen	Core area A_c (mm ²)	Core yield strength σ_{cy} (N/mm ²)	Restrainer stiffness E_{IB} (kNm ²)	Lower spring K_{Rg1} (kNm)	Upper spring K_{Rg2} (kNm)	Upper GL spring $K_{Rg2'}$ (kNm)	Beam Spring K_{Rb} (kNm)	Connection stiffness* $\gamma_j EI_B$ (kNm ²)	Total length L_0 (mm)	Insert length L_{in} (mm)	Plastic zone length L_p (mm)	Lower connection length $\xi_1 L_0$ (mm)	Upper connection length $\xi_2 L_0$ (mm)	Clearance s_r (mm)	upper normalized spring ξK_{Rg2}
H-RN2	1080	293	1080	11426	3153	3585	26174	696	2460	180	1044	454	602	1.0	2.73
M-CN2	1080	293	1500	11426	1691	3585	3202	696	2460	180	1044	454	602	1.0	1.46
L-RN'2	1080	293	1080	306	221	351	598	696	2460	180	1044	454	602	1.0	0.19
L-RF2	1080	293	1080	306	221	351	598	696	2460	180	1044	454	602	1.0	0.19
L-CC2	1080	293	1500	306	221	351	598	696	2460	180	1044	454	602	1.0	0.19
L-RN0	1080	293	1080	306	221	351	598	696	2460	0	1404	454	602	1.0	0.19

*Contribution of the splice plate section to the connection stiffness is neglected

strength=293 MPa), and the core cross-section size A_c was 12×90 mm. The restrainer is either a mortar-filled square box section with the width of 125 mm and thickness of 4.5 mm, or a circular tube with an external diameter of 165.2 mm and tube wall thickness of 4.5 mm. Three connection types of upper secondary beams as shown in Figure 7, combined with the gusset plates as shown in Figure 8, were used in the tests: the high-stiffness connection ($\xi K_{Rg2} = 2.73$), the medium-stiffness connection ($\xi K_{Rg2} = 1.46$), and the low-stiffness connection ($\xi K_{Rg2} = 0.19$). The specimens were labelled as (H, M, or L: stiffness at the upper connection)-(R: rectangular restrainer, C: circular restrainer)-(N: no reinforcement, F: ribs, C: collars)-2 (ratio of the insert zone length to the core plate width). Rotational stiffness of each combination was measured experimentally using the test frame (Appendix C). For the low-stiffness type, restrainer end reinforcements were attached to RF2 with ribs and CC2 with collars as in Figure 9 (iv) and (v). The fabrication of BRBs and gusset plates were carried out under AIJ/JASS6 specifications, and the initial imperfection of the specimen was confirmed less than 1/2000 of the length. This value was counted in the stability assessment. Prior to each test, an out-of-plane displacement equivalent to 1% radian story drift was applied to each specimen. For cyclic loading, up to 3% normalized axial deformation ($\varepsilon_n = \delta/L_p$) was applied, according to the loading protocol shown in Figure 6. Here, the normalized axial deformation, which is approximately equivalent to the story drift angle, is the ratio of the axial deformation to the plastic length, L_p , of the core plate. After $\varepsilon_n = 3.0\%$, the same amplitude was used until fracture.

The hysteresis loops obtained from the cyclic loading tests for each specimen are shown in Figure 10. The axial stress is defined as the axial force divided by the initial core section area. Each figure also shows the cumulative plastic deformation, $\Sigma \Delta \varepsilon_p = \Sigma \Delta \delta_p / L_p$, and the normalized cumulative absorbed energy, $\chi_w = E_d / \sigma_y A_c$, until instability. Specimen H-RN2 (Figure 10 (a)), with the high-stiffness connection, showed stable hysteretic behavior until the core plate fractured after the 18th cycle of 3% normalized axial deformation. Similarly, specimen M-CN2 (Figure 10 (b)), with a medium-stiffness connection, showed stable hysteresis until the 18th cycle of 3% normalized axial deformation. This performance would easily satisfy the requirement for energy-dissipating braces. Specimen L-RN'2 (Figure 10 (c)), which has a low-stiffness connection with weaker restrainer-ends, showed stable hysteresis until the second cycle at 3% normalized axial deformation, after which out-of-plane instability occurred. The specimen started buckling in the asymmetrical mode as shown in Figure 10 (g), agreeing with the predicted failure mechanism. Even under the same low stiffness beam conditions, the specimens with restrainer-end reinforcements (L-RF2, L-CC2) showed stable hysteresis of 3% normalized axial deformation until the core plate fractured at the 18th and 15th cycles, respectively, as shown in Figure 10 (d) and (e). This means that the restrainer-end reinforcements are effective in enhancing the stability limits. In L-CC2, friction between the collar and the restrainer caused slight strength increase at 3% compression. Specimen L-RN0 (Figure 10 (f)), which has the low-stiffness gusset plates without an insert zone length, showed a



(h) Out-of-plane displacement in L-RN'2 and L-RN0
 Figure 10 Normalized axial force–deformation relationship

stable hysteresis loop until only the first cycle of 0.5% normalized axial deformation, after which it experienced out-of-plane instability associated with hinging at the neck in a similar mode as L-RN'2. These test results indicate that the stability of a BRB with a chevron configuration is significantly affected by the rotational stiffness of the attached beams and the strength of the restrainer ends, as the proposed equations predicted. Figure 10 (h) shows the out-of-plane displacement transitions at the upper and the lower restrainer ends in the collapsed specimens of L-RN'2 and L-RN0. Both show larger amplitudes at the upper restrainer ends prior to instability, which indicates that these specimens collapsed in an asymmetric mode with larger displacements at the upper connections as shown in Figure 5 (b).

In order to confirm the validity of the proposed equations, each specimen was evaluated using Equations (4), (20), and (24)–(27). The restrainer moment transfer capacity, M_p^r , of each specimen was estimated using the same equations as those in the previous study [1]. In Table 2, the estimated values of the stability limit, N_{lim} , are compared with the maximum axial loads obtained from the tests. It is observed that the expected stability limits of collapsed specimens L-RN'2 and L-RN0 were 371 kN and 256 kN, respectively, which were lower than the expected

Table 2 Stability evaluations using proposed equation

Specimen	Bending moment				Elastic buckling strength N_{cr}^B (kN)	Initial imperfection a_r (mm)	Connection buckling strength N_{cr}^r (kN)	Slender-ness ratio λ_r	Connec-tion radius i_r (mm)	Core yield strength N_{cu} (kN)	Stability limit				Experimental results N_{lim}^{exp} (kN)
	Restrainer ends M_p^r (kNm)	Initial M_0^r (kNm)	Lower GPL M_p^{g1} (kNm)	Upper GPL M_p^{g2} (kNm)							Calculated				
											Elastic N_{lim1} (kN)	Plastic N_{lim2} (kN)	Min. N_{lim} (kN)	Judge N_{lim} > N_{cu}	
H-RN2	4.27	0.0	355	274	5241	4.0	428	63	31.3	475	1237	4717	1237	OK	No collapse
M-CN2	4.27	0.0	355	274	4369	4.8	389	75	31.3	475	1060	3932	1060	OK	No collapse
L-RN'2	1.75	0.0	2.48	2.49	2151	5.6	112	170	31.3	475	370	450	370	NG	527
L-RF2	23.0	0.0	2.48	2.49	2151	4.0	112	170	31.3	475	1595	1591	1591	OK	No collapse
L-CC2	45.1	0.0	2.48	2.49	2054	5.0	112	170	31.3	475	1693	1683	1683	OK	No collapse
L-RN0	0.51	0.0	2.48	2.49	2151	3.1	112	170	31.3	475	257	485	257	NG	339

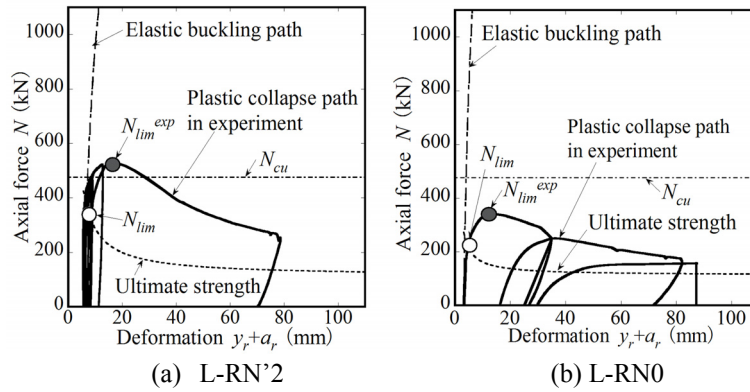


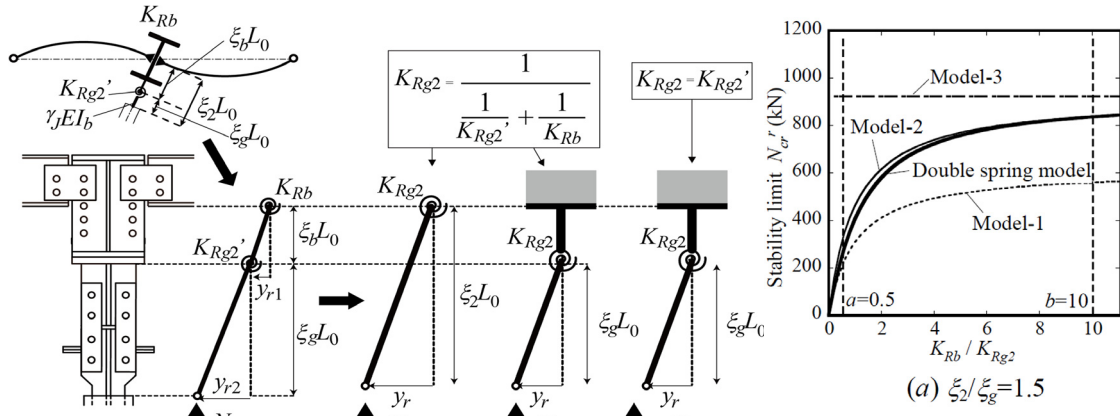
Figure 11 Relationship between axial force and out-of-plane displacement

BRB design axial force $N_{cu} = 1.5 \times A_c \times \sigma_{cy} = 475$ kN. The N_{lim} values of all other specimens exceeded the design axial force N_{cu} of 475 kN, which satisfactorily demonstrated stable hysteresis. Figure 11 shows a comparison between the measured axial force–displacement relationships of the collapsed specimens and those obtained using Equations (4) and (20). Although the test results that exceeded the stability limit had larger force–displacement relationships than those obtained using the proposed equations, the stiffness degradation points generally agreed with the predicted strength, and their force-displacement paths after the collapse tended to fall in parallel to the estimated collapse path.

4 STABILITY DESIGN OF BRB WITH CHEVRON CONFIGURATION

Although the proposed equations can be used to evaluate the stability of BRBs in chevron configurations, the equations are too conservative in cases where the rotational stiffness of the upper beam K_{Rb} is high. This is because of the simplification in taking a single spring at the beam center instead of two springs as shown in Figure 4 (a). Where rotational stiffness of the beam is relatively high, the rotation of the connection is observed to start near the bottom of the beam. Here, an additional approach using simplified models for evaluating these effects is proposed. When the moment transfer capacity at the restrainer-ends is negligible, the precise stability limit of the symmetrical collapse mode is determined by using the double-spring model of the beam rotation and upper connection flexure as shown in Figure 12(a). Further simplifications representing special conditions are shown in Figures 12(b)–(d).

When the rotational stiffness of the upper beam is low ($K_{Rb} < aK'_{Rg2}$), the spring should be placed at the beam center as in Model-1 (Figure 12(b)). The rotational stiffness of the upper connections should be evaluated using Equation (5), the connection length should be evaluated as $\xi_2 L_0$, and Equations (1) and (24)–(27) should be used for stability evaluation. However,



(a) Double-spring model, (b) Model-1, (c) Model-2, (d) Model-3
Figure 12 Mechanical model at upper connection

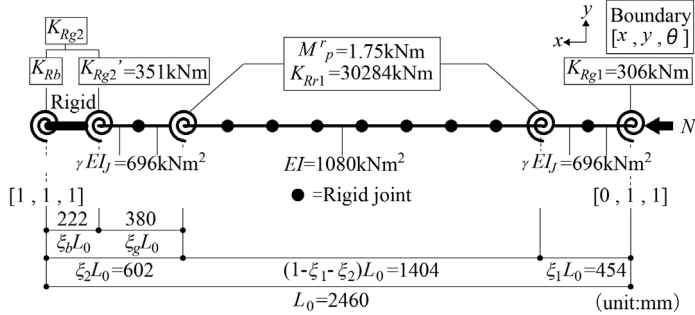
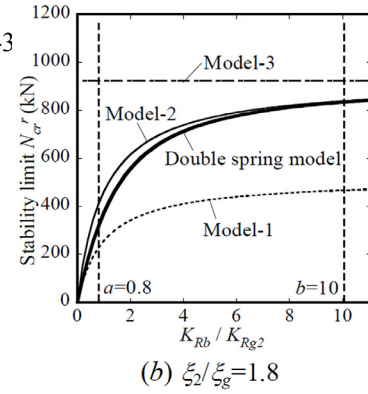


Figure 14 Full model $\xi_2/\xi_g = 1.6$



(b) $\xi_2/\xi_g = 1.8$
Figure 13 Stability limit for connection model

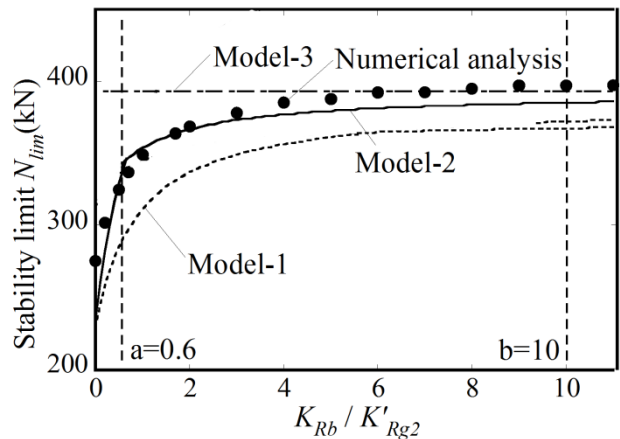


Figure 15 Simplified models vs. accurate model

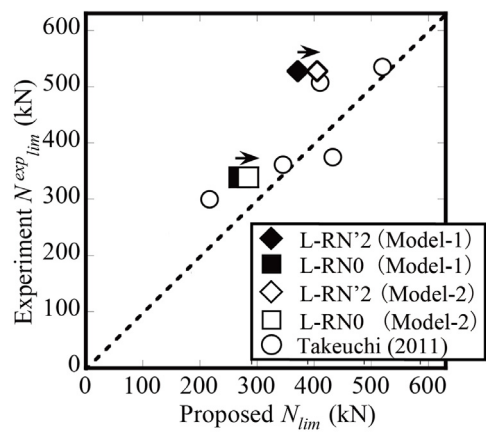


Figure 16 Accuracy of proposed method

when the rotational stiffness of the upper beam is considerably higher ($aK'_{Rg2} < K_{Rb} < bK'_{Rg2}$), Model-2 (Figure 12(c)) can be used, with the spring placed at the bottom of the beam. The beam rotation may be neglected and Model-3(Figure 12(d)) used when the rotational stiffness of the upper beam is extremely high ($bK'_{Rg2} < K_{Rb}$) due to stiff perpendicular secondary beams, floor slabs, and other elements. The stability limits of the models in Figures 12(a)–(d) is expressed in the following equations.

Note that from Equation (1), N_{lim1} (symmetric) becomes the same as N_{cr}^r when $M_p^r = 0$.

$$N_{lim1} = N_{cr}^r = \frac{(\xi_2 L_0 K'_{Rg2} + \xi_g L_0 K_{Rb}) - \sqrt{(\xi_2 L_0 K'_{Rg2} + \xi_g L_0 K_{Rb})^2 - 4(\xi_g L_0)(\xi_b L_0) K'_{Rg2} K_{Rb}}}{2(\xi_g L_0)(\xi_b L_0)} \quad (Double-spring \ model: \ Figure \ 11(a)) \quad (28)$$

$$N_{lim1} = N_{cr}^r = \frac{K_{Rg2}}{\xi_2 L_0} = \frac{1}{\frac{1}{K_{Rg2}'} + \frac{1}{K_{Rb}}} \frac{1}{\xi_2 L_0} \quad (Model-1: \ Figure \ 11(b)) \quad (29)$$

$$N_{lim1} = N_{cr}^r = \frac{K_{Rg2}}{\xi_g L_0} = \frac{1}{\frac{1}{K_{Rg2}'} + \frac{1}{K_{Rb}}} \frac{1}{\xi_g L_0} \quad (Model-2: \ Figure \ 11(c)) \quad (30)$$

$$N_{lim1} = N_{cr}^r = \frac{K_{Rg2}'}{\xi_g L_0} \quad (Model-3: \ Figure \ 11(d)) \quad (31)$$

The stability limits derived from Equations (28)–(31) are compared in Figures 13(a) and 13(b) for different ξ_2/ξ_g ratios. The values obtained by Equation (28) are close to those obtained from Equation (29) in a range of relatively low K_{Rb}/K'_{Rg2} ratios. However, these values reach those obtained from Equation (30) at medium K_{Rb}/K'_{Rg2} ratios, and both sets of values approach those obtained from Equation (31) at high K_{Rb}/K'_{Rg2} ratios. In this study, we propose the following limit values for K_{Rb}/K'_{Rg2} to determine the applicable range for the simplified Models 1~3:

$$a = \xi_2/\xi_g - 1, \quad b = 10 \quad (32), (33)$$

These limits are indicated in Figure 13.

Evaluation using numerical models consisting of beam elements as shown in Figure 14 was performed, including the effects of moment transfer capacity at the restrainer ends. The configuration of the models is based on the specimen L-RN'2, and elasto-plastic springs are introduced at the restrainer-ends. Asymmetrical imperfections based on experimental measurements noted in Table 1 were applied, and stability limits were evaluated by push-over analysis for each K_{Rb}/K'_{Rg2} ratio, including geometrical non-linearity. The evaluation results are illustrated in Figure 15, where they are compared with the results of the proposed method. In the proposed equations, one-sided and asymmetrical modes of Model-1 evaluations provide one of the smallest stability limits, asymmetrical modes of Model-3 evaluations have the highest limits, and the limits of Model-2 evaluations fall in between. In this case, the numerical analysis results are close to Model-1 where $K_{Rb}/K'_{Rg2} < a = \xi_2/\xi_g - 1 = 0.6$, close to Model-2 where $0.6 < K_{Rb}/K'_{Rg2} < 10$, and close to Model-3 where $10 < K_{Rb}/K'_{Rg2}$. This implies the evaluated borders a and b appropriately assess the stability limit of BRBs in the chevron configuration.

The K_{Rb}/K'_{Rg2} value in the specimens L-RN'2 and L-RN0 was 1.70 from Table 1, which is larger than $a = \xi_2/\xi_g - 1 = 0.6$ and less than 10. This indicates that these specimens can be evaluated with Model-2, instead of Model-1. Figure 16 shows a comparison of the estimated stability limit N_{lim} using Model-1 (■◆) and Model-2 (□◇), with the peak axial force obtained from the experimental tests, and also from the results of the previous study (○) [1]. By using Model-2, calculation accuracy is slightly improved over Model-1. In general, the results obtained using the proposed equations are consistent with the experimental results, and the method of selecting the connection models by the stiffness ratios of attached beams is considered valid.

The following process can be applied in practice to ensure BRB stability.

- 1) The simplified BRB Model-1 to 3 is selected from the condition of Equation (32) and (33).
- 2) N_{cr}^r is determined by applying the larger equivalent slenderness ratio from Equation (24) and (25) into design column curves. Then N_{lim1} is calculated by Equation (1).
- 3) N_{lim2} is calculated from the smaller of Equation (26) and (27). Then the stability limit, N_{lim} , is evaluated as the smaller of N_{lim1} and N_{lim2} .
- 4) If N_{lim} is larger than expected yield axial force of the core, N_{cu} , BRB stability is secured. If not, increase K_{Rb} , K'_{Rg} , or M_p^r and repeat steps 1 to 4.

5 CONCLUSIONS

In this study, the authors' previously proposed method for stability evaluation of BRBs, including bending-moment transfer capacity at restrainer ends, was extended to the use of BRBs under asymmetrical conditions in chevron configurations. A compact equation set was established to evaluate global BRB stability under asymmetrical conditions. A series of cyclic loading tests were conducted on BRBs in a chevron configuration, and the results were compared with those obtained using the extended method of stability evaluation. The resulting conclusions are summarized as follows:

- 1) In the cyclic loading tests of BRBs in a chevron configuration, specimens with low upper-beam stiffness experienced out-of-plane instability before achieving stable hysteresis until core fracture, whereas specimens with restrainer-end reinforcements under the same conditions showed stable hysteresis. This may be attributed to the fact that the stiffness of the upper connection and the restrainer moment transfer capacity both significantly influence BRB stability.
- 2) The extended method of the stability evaluation is applicable to the direct estimation of the stability limit strength of BRBs regardless of the configuration. The obtained results demonstrate that the evaluated stability limit strengths align well with the experimental results of collapsed specimens, thus validating the proposed equations.
- 3) In order to facilitate the stability evaluation of BRBs, three simple evaluation models were proposed for upper connections, applicable for specific ranges of stiffness ratio between the upper beam and the upper gusset plate.

ACKNOWLEDGEMENTS

The authors would like to acknowledge the support of Nippon Steel and Sumikin Engineering Co. Ltd, Nikken Sekkei Co. Ltd, and great contributions of Dr. Yoshinao Konishi, Mr. Hitoshi Ozaki, and Mr. Benjamin Sitler for this study.

NOTATIONS

- a, b : border constant for the beam stiffness
 a_r : total initial imperfection: $a_r = a_i + e + s_r + (2s_r/L_{in})\xi L_0$, a_i : maximum imperfection along the restrainer, e : axial force eccentricity, s_r : clearance between core and restrainer
 y_{r1} : out-of-plane deformation at column-side restrainer end
 y_{r2} : out-of-plane deformation at beam-side restrainer end
 y_{rel} : additional out-of-plane deformation due to bending of connection zone at the column-side end

y_{re2} :	additional out-of-plane deformation due to bending of connection zone at the beam-side end
y_{rs1} :	additional deformation due to the column-side end spring rotation
y_{rs2} :	additional deformation due to the beam-side end spring rotation
A_c :	core plate cross-section
B_c :	core plate width
EI_B :	bending stiffness of restrainer
E_d :	absorbed hysteretic energy until instability or fracture
K_{Rb} :	rotational spring stiffness of attached beam
K_{Rg1} :	rotational spring stiffness at column-side gusset plate
K'_{Rg2} :	rotational spring stiffness at beam-side gusset plate
K_{Rg2} :	rotational spring stiffness at beam-side gusset plate, including stiffness of the attached beam
L_{in} :	insert zone length
L_p :	plastic zone length of core plate
M_0^r :	additional bending moment derived from story out-of-plane drift
M_y^B :	bending strength of restrainer
M_p^g :	plastic bending strength of gusset plate including axial force effect
M_p^r :	bending-moment transfer capacity at restrainer end
N :	axial force
N_{cu} :	maximum axial strength of core plate
N_{cr}^B :	global elastic buckling strength of BRB including effect of gusset plate rotational stiffness
N_{cr}^r :	global elastic buckling strength with pin conditions at restrainer ends
N_{lim} :	expected stability limit axial force
N_{lim1} :	expected stability limit axial force assuming elastic gusset plates
N_{lim2} :	expected stability limit axial force assuming plastic hinges at gusset plates
N_{cu} :	ultimate axial strength of cruciform core plate at neck
N_y :	yield axial force of core plate
T :	external work
U_p :	plastic strain energy stored in plastic hinges
U_s :	energy stored in springs
U_e :	strain energy stored in both connection zones
$\gamma_J EI_B$:	bending stiffness of connection zone
δ_0 :	story out-of-plane drift
δ :	axial deformation
δ_p :	axial plastic deformation
$\xi_1 L_0$:	connection zone length at column-side
$\xi_2 L_0$:	connection zone length at beam-side
$\Delta\theta_{r1}$:	rotational angle of plastic hinge at column-side restrainer end
$\Delta\theta_{r2}$:	rotational angle of plastic hinge at beam-side restrainer end
$\Delta\theta_{s1}$:	rotation at column-side gusset plate
$\Delta\theta_{s2}$:	rotation at beam-side gusset plate
Δu_g :	axial deformation
ξK_{Rg1} :	normalized rotational stiffness for column-side gusset plate ($=K_{Rg1} \xi_1 L_0 / \gamma_J EI_B$)
ξK_{Rg2} :	normalized rotational stiffness for beam-side gusset plate ($=K_{Rg2} \xi_2 L_0 / \gamma_J EI_B$)
λ_r :	equivalent slenderness ratio for global elastic buckling strength, with pin conditions at restrainer ends
$\Sigma \Delta \varepsilon_p$:	normalized cumulative plastic deformation ($=E_d / \sigma_y A_c$)

σ_{cy} : yield stress of core plate material
 σ_{ry} : yield stress of restrainer tube material
 σ_n : normalized stress of BRB ($= N/A_c$)

REFERENCES

1. Takeuchi T, Ozaki H, Matsui R, Sutcu F. Out-of-plane stability of buckling-restrained braces including moment transfer capacity. *Earthquake Engineering & Structural Dynamics* 2014; **43**(6): 851–869. DOI: 10.1002/eqe.2376
2. Chou C C, Chen P J. Compressive behavior of central gusset plate connections for a buckling-restrained braced frame. *Journal of Constructional Steel Research* 2009; **65**(5): 1138–1148. DOI:10.1016/j.jcsr.2008.11.004
3. Chou C C, Liu J H, Pham D H. Steel buckling-restrained braced frames with single and dual corner gusset connections: seismic tests and analyses. *Journal of Earthquake Engineering and Structural Dynamics* 2012; **41**(7): 1137–1156. DOI: 10.1002/eqe.1176
4. Eryasar M E, Topkaya C. An experimental study on steel-encased buckling-restrained brace hysteretic dampers. *Earthquake Engineering and Structural Dynamics* 2010; **39**(5): 561–581. DOI: 10.1002/eqe.959
5. Hikino T, Okazaki T, Kajiwara K, Nakashima M. Out-of-plane stability of buckling-restrained braces. *Proceedings of ASCE Structural Congress* 2011;938-949. DOI:10.1061/41171(401)83
6. Ji X, Hikino T, Kasai K, Nakashima M. Damping identification of full-scale passively controlled five-story steel building structure. *Earthquake Engineering and Structural Dynamics*, 2013; 42:277–295. DOI: 10.1002/eqe.2208
7. Koetaka Y, Kinoshita T, Inoue K, Iitani K. Criteria of buckling-restrained braces to prevent out-of-plane Buckling. *Proceedings of 14th World Conference on Earthquake Engineering* 2008.
8. Lin P C, Tsai K C, Wang K J, Yu Y J, Wei C Y, Wu A C, Tsai C Y, Lin C. H, Chen J C, Schellenberg A H, Mahin S, Roeder C W. Seismic design and hybrid tests of a full-scale three-story buckling-restrained braced frame using welded end connections and thin profile. *Earthquake Engineering and Structural Dynamics* 2012; **41**(9): 1001–1020. DOI: 10.1002/eqe.1171
9. Matsui R, Takeuchi T, Nishimoto K, Takahashi S, Ohyama T. Effective buckling length of buckling restrained braces considering rotational stiffness at restrainer ends. *7th International Conference on Urban Earthquake Engineering & 5th International Conference on Earthquake Engineering Proceedings* 2010; 1049–1058.
10. Okazaki T, Hikino T, Kajiwara K. Out-of-Plane stability of buckling-restrained braces. *Proceeding of 15th World Conference on Earthquake Engineering* 2012.
11. Tsai K C, Hsiao P C. Pseudo-dynamic test of a full-scale CFT/BRB frame-Part II: Seismic performance of buckling-restrained braces and connections. *Earthquake Engineering and Structural Dynamics* 2008; **37**:1099–1115. DOI: 10.1002/eqe.803
12. Wigle V R, Fahnestock L A. Buckling-restrained braced frame connection performance. *Journal of Constructional Steel Research* 2010; **66**(1): 65–74. DOI:10.1016/j.jcsr.2009.07.014
13. Zhao J, Wu B, Ou J. A novel type of angle steel buckling-restrained brace: Cyclic behavior and failure mechanism. *Earthquake Engineering and Structural Dynamics* 2011 **40**(10), 1083–1102. DOI: 10.1002/eqe.1071
14. Zhao J, Wu B, Ou J. Flexural demand on pin-connected buckling-restrained braces and design recommendations. *Journal of Structural Engineering* 2011; 138(11): 1398-1415. DOI.org/10.1061/(ASCE)ST.1943-541X.0000549
15. AISC341-10: Seismic provisions for structural steel buildings, 2010, F4: Buckling-Restrained Braced Frames.
16. Architectural Institute of Japan: Recommendations for Stability Design of Steel Structures, Sec. 3.5

- Buckling-restrained Braces, 2009, 74–79.
17. Lin P-C, Tsai, K-C, Wu A-C, Chuang M-C. Seismic design and test of gusset connections for buckling-restrained braced frames. *Earthquake Engineering and Structural Dynamics*, 2014; **43**(4): 565–587. DOI: 10.1002/eqe.2360
 18. Zhao J, Wu B, Qu J. A practical and unified global stability design method of buckling-restrained braces: Discussion on pinned connections. *Journal of Constructional Steel Research* 2014; **95**(4) 106–115. DOI:10.1016/j.jcsr.2013.12.001
 19. Bruneau M, Uang C M, Sabelli R S E. Ductile design of Steel Structures, Chap.11, Ductile design of Buckling-restrained frames, 2nd edition McGraw-Hill, 2011
 20. Palmer K D, Christopoulos A S, Lehman D E, Roeder C W. Experimental evaluation of cyclically loaded, large-scale, planar and 3-D buckling-restrained braced frames. *Journal of Constructional Steel Research* 2014; **101**(10): 415–425. DOI:10.1016/j.jcsr.2014.06.008
 21. Ida M, Takeuchi T, Matsui R, Konishi Y, et al. Stability Assessment of Buckling Restrained Braces Taking Connections into Account (Part.2 Evaluation of Rotational Stiffness of Brace Connections), *Proceedings of AIJ annual meeting, Structure-III* 2013; 22624: 1247-1248. (in Japanese)
 22. Kinoshita T, Koetaka Y, Inoue I, Iitani K. Out-of-plane stiffness and yield strength of cruciform connections for buckling-restrained braces, *AIJ Journal of structural and constructional engineering* 2008; **73**(632): 1865-1873. DOI.org/10.3130/aijs.73.1865. (in Japanese)
 23. Ohyama S, Takeuchi T, et al. Stability Assessment of Buckling Restrained Braces Taking Connections into Account, (Part.15 Calculation Methods of Rotational Stiffness of Brace Connections in Chevron Configuration), *Proceedings of AIJ annual meeting, Structure-III* 2015; 22548: 1095-1096. (in Japanese)

APPENDIX A:

ESTIMATION OF THE BENDING MOMENT PRODUCED BY OUT-OF-PLANE DRIFT

The initial bending moment M_0^r at the restrainer ends produced by out-of-plane drift can be estimated from numerical analyses using the model as shown in Figure A1 or by using the following equation, which takes $\xi K_{Rg} = \max[\xi K_{Rg1}, \xi K_{Rg2}]$, and $\xi^r = \min[\xi^r_1, \xi^r_2]$.

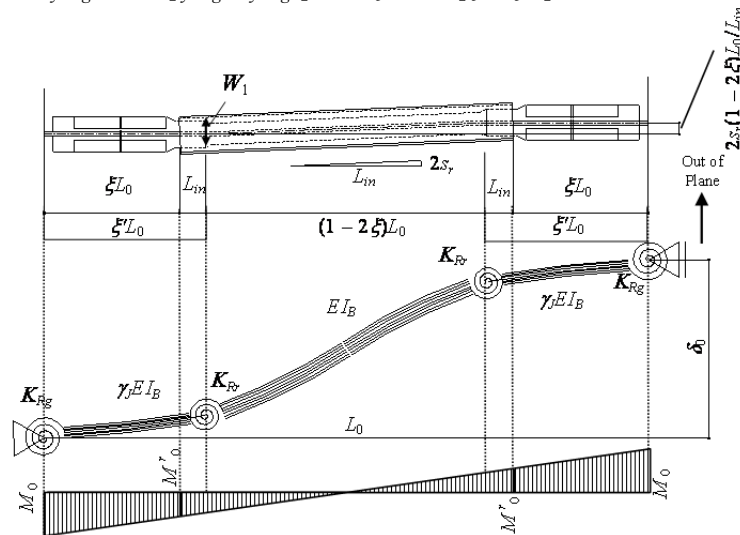


Figure A1 Bending moment produced by out-of-plane drift

$$M_0^r = (1-2\xi) \left\{ \frac{\delta_0}{L_0} - \frac{2s_r}{L_{in}} (1-2\xi) \right\} \cdot \frac{EI_B}{L_0} \cdot \frac{6\gamma_J}{2\xi'(3-6\xi'+4\xi'^2) + \gamma_J(1-2\xi')^3 + \frac{6\xi}{\xi K_{Rg}} + \frac{6\gamma_J(1-2\xi')^2}{L K_{Rr}}} \geq 0 \quad (A1)$$

where,

$$\xi K_{Rg} = \frac{K_{Rg} \xi L_0}{\gamma_J EI_B}, \quad L K_{Rr} = \frac{K_{Rr} L_0}{EI_B}, \quad \xi' = \xi + \frac{L_{in}}{L_0} \quad (A2)$$

K_{Rg} is the rotational spring at the gusset plates and K_{Rr} is the rotational spring at the restrainer ends. When K_{Rr} and EI_B/L_0 become infinity, $\gamma = 1$ and $\xi' = \xi$, this equation approaches the simpler formulas from the previous study (Equation (31) in Reference [1]) as follows.

$$M_0^r = (1-2\xi) \left\{ \frac{\delta_0}{L_0} - \frac{2s_r}{L_{in}} (1-2\xi) \right\} K_{Rg} \geq 0 \quad (A3)$$

M_0^r becomes zero when $\frac{\delta_0}{L_0} \leq \frac{2s_r}{L_{in}} (1-2\xi)$, from Equations (A1) and (A3).

APPENDIX B:

ESTIMATION OF GLOBAL ELASTIC BUCKLING STRENGTH OF A BRB

The global elastic buckling strength of a BRB, N_{cr}^B , including the effects of the connection zone's bending stiffness and the gusset plates' rotational stiffness, can be estimated from numerical analysis, using the model shown in Figure B1, or by using the following equations, which take $K_{Rg} = \min[K_{Rg1}, K_{Rg2}]$, and $\xi = \max[\xi_1, \xi_2]$.

$$N_{cr}^B = \alpha^2 EI \quad (B1)$$

where, α is the value satisfying the following equations.

$$\begin{aligned} & \alpha^3 (EI_B)^2 L_0 S_1 S_4 - \alpha^2 EI_B L_0 \left(K_{Rr} S_1 C_4 + \frac{K_{Rg} + K_{Rr}}{\sqrt{\gamma_J}} C_1 S_4 \right) + 2\alpha EI_B K_{Rg} S_1 S_4 \\ & + \alpha K_{Rg} K_{Rr} L_0 \left(\frac{1}{\sqrt{\gamma_J}} C_1 C_4 - \frac{1}{\gamma_J} S_1 S_4 \right) - 2K_{Rg} K_{Rr} \left(S_1 C_4 + \frac{1}{\sqrt{\gamma_J}} C_1 S_4 \right) = 0 \quad (B2) \\ & S_1 = \sin \frac{\alpha}{\sqrt{\gamma_J}} \xi L_0, C_1 = \cos \frac{\alpha}{\sqrt{\gamma_J}} \xi L_0, S_4 = \sin \alpha L_0 \left(\frac{1}{2} - \xi \right), C_4 = \cos \alpha L_0 \left(\frac{1}{2} - \xi \right) \end{aligned}$$

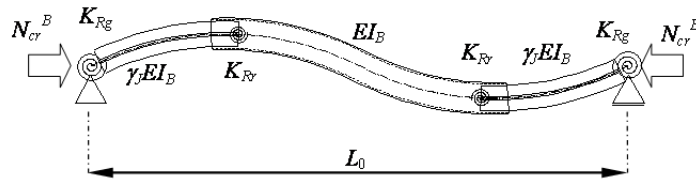


Figure B1 Buckling mode including springs

When K_{Rr} is infinity and $\gamma_J = 1$, the solution approaches the simpler approximate formula in the previous study [1].

$$N_{cr}^B = \frac{4\pi^2 EI_B \cdot {}_L\kappa_{Rg}^2 + 10 \cdot {}_L\kappa_{Rg} + 16}{L_0^2 \cdot {}_L\kappa_{Rg}^2 + 14 \cdot {}_L\kappa_{Rg} + 64} \quad (B3)$$

where, ${}_L\kappa_{Rg} = \frac{K_{Rg} L_0}{EI_B}$. N_{cr}^B becomes $\pi^2 EI_B / L_0^2$ when ${}_L\kappa_{Rg} = 0$, and $N_{cr}^B = 4\pi^2 EI_B / L_0^2$ when ${}_L\kappa_{Rg} = \infty$.

APPENDIX C:

ESTIMATION OF ROTATIONAL STIFFNESS OF THE UPPER BEAM

The rotational spring stiffness of the gusset plate, K_{Rg2} , and upper beam, K_{Rb} , in Table 1 were obtained directly by experiments prior to specimen loading as shown in Figure C1. This includes the gusset plate deformation, the torsional stiffness of the main beam, the torsional stiffness given by rigidly connected secondary beams perpendicular to the main beam, the bending stiffness of the other BRB in tension, and the bending deformation of the main beam section along weak axis. For practical design, an easy evaluation method for calculation of the gusset plate stiffness, K'_{Rg} , is proposed in reference [22]. Also, an evaluation method for calculation of torsional stiffness of the main beam is proposed as follows in reference [23], whose validity is confirmed by FEM analyses.

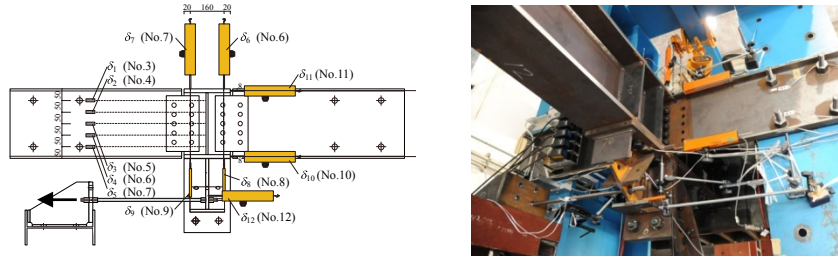


Figure C1 Experimental evaluation of rotational spring stiffness

The rotational springs of upper beams K_{Rb} can be derived as follows.

$$K_{Rb} = K_{RbT} + K_{RbSB} \quad (C1)$$

where, K_{RbT} is the torsional stiffness of the main beam the BRB is attached on, and K_{RbSB} is the torsional stiffness provided by the rigidly connected secondary beams perpendicular to the main beam. Equation (C1) neglects the bending stiffness of the other BRB in tension and the floor slab, and assumes that the main beam rotates in torsion as a rigid body. K_{RbT} can be estimated by the following equation.

$$K_{RbT} = \frac{2GJ\nu}{\left\{ \frac{(\cosh \nu l_G - 1)^2}{\sinh \nu l_G} - \sinh \nu l_G + \nu l_G \right\}}, \quad \nu = \sqrt{\frac{GJ}{EI}} \quad (C2)$$

Where, l_G is the half length of attached main beam as shown in Figure C2, and GJ and EI are Saint-Venant's torsional stiffness and bending torsional stiffness of the main beam, respectively.

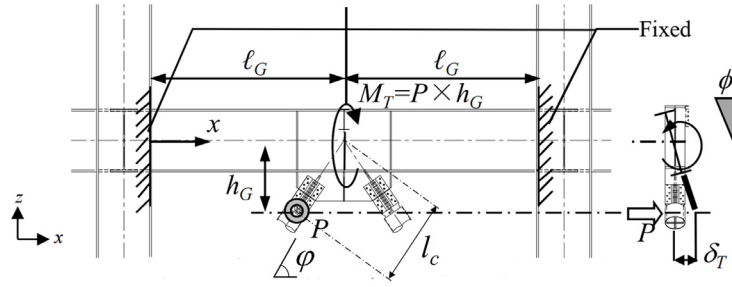


Figure C2 Rotational spring of attached beam

K_{RbSB} can be estimated by the following equation.

$$K_{RbSB} = \frac{3EI_{SB}}{l_{SB}} \left(\frac{l_c}{h_{SB}} \right)^2 \quad (C3)$$

where, l_{SB} is the length of secondary beam, EI_{SB} is bending stiffness of secondary beam, and h_{SB} is the vertical distance from the restrainer end to the center of the secondary beam as shown in Figure C3. l_c is the connection length along the brace from the center of the main beam as in Figure C2.

The above estimation formula can be used where the BRB connection point is placed at the center of the main beam, is detailed with stiffeners, and the vertical deflection of the other end of secondary beam is restrained. When a concrete floor slab is attached on the main beam, the above method gives conservative values. The method is also valid for situations requiring a large void adjacent to the main beam.

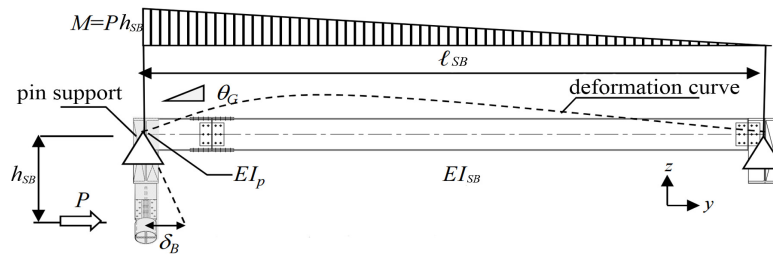


Figure C3 Effect of out-of-plane secondary beam